

RESEARCH PAPER

Neurospectral modeling of rectangular patch with rectangular aperture in the ground plane

LOTFI DJOUANE¹, SAMI BEDRA², RANDA BEDRA² AND TAREK FORTAKI²

In this study, we propose an artificial neural network in conjunction with spectral domain approach (SDA), for fast and accurate determination of the resonant frequency and half-power bandwidth of rectangular patch over the ground plane with rectangular aperture. The performances evaluation of the neurospectral method reveals superiority over the conventional SDA model in terms of errors and time. The results obtained from the neurospectral method are in very good agreement with the experimental and theoretical results available in the literature. Finally, numerical results for the effect of rectangular aperture dimensions on the resonant characteristics of the rectangular patch are also investigated.

Keywords: Microstrip antenna, Artificial neural network, Design and modeling, Spectral domain

Received 31 January 2013; Revised 23 June 2014; Accepted 27 June 2014; first published online 24 July 2014

I. INTRODUCTION

Microstrip patch antennas are used in the wide range of applications such as aircraft, satellite, missiles, and land vehicles and in small portable wireless communication equipment's due to their compactness, light weight, low-profile, and relative ease of fabrication method [1–3]. The main shortcomings of these antennas are narrow bandwidth and low gain. These shortcomings can be overcome in by proper design of an antenna, and especially using proper substrate thickness and dielectric constant as well as a proper way of feeding [4]. Various techniques have been proposed to improve the bandwidth operation of the microstrip elements, and the most common technique using feeding according element through an aperture cut in a microstrip line ground plane [5, 6]. Alternatively, aperture-coupling feeds are gaining popularity owing to a number of advantages, such as a greater bandwidth and efficiency, weak parasitic radiation in the useful direction with respect to conventionally feed antennas and optimal performance for both the feeding network and antenna element [5]. With the increasing complexity of geometry and material property, designing these antennas requires more and more dedicated and sophisticated computer-aided-design (CAD) tools to predict the characteristics [7]. Various methods and commercial software are available for analysis and synthesis of microstrip antennas. These commercial design packages use computer intensive numerical methods such as, finite-element method, method

of moment (MoM), finite-difference time-domain method, etc. These techniques require high computational resources and also take lots of computation time [8]. In the present-day scenario, neural network models are used extensively for wireless communication engineering, which eliminate the complex and time-consuming mathematical procedure of designing, such as the MoMs [9]. The neural networks in conjunction with spectral domain approach (SDA) was firstly proposed by Mishra and Patnaik [10], to calculate the complex resonant frequency and the input impedance [11] of rectangular microstrip antenna, this approach is named neurospectral method [12]. This is the main reason for selecting the neurospectral to estimate the resonant frequency and half-power bandwidth of a rectangular microstrip patch over the ground plane with rectangular aperture. To the best of the author's knowledge, the artificial neural network (ANN) models for predicting the characteristics of microstrip patches over the ground plane with rectangular aperture have not been thoroughly reported in the open literature.

The objective of this work is to present an integrated approach based on ANNs and SDA. We introduce the ANNs in the analysis of a rectangular microstrip patch over a ground plane with rectangular aperture to reduce the complexity of the spectral approach and to minimize the central processing unit (CPU) time necessary to obtain the numerical results. The neurospectral model is simple, easy to apply, and very useful for antenna engineers to predict both resonant frequency and half-power bandwidth.

II. THEORETICAL FORMULATION

The geometry of the considered structure is shown in Fig. 1. We have a rectangular microstrip patch of length L_p along

¹Electronics Department, University of M'sila, 28000 M'sila, Algeria

²Electronics Department, University of Batna, 05000 Batna, Algeria

Corresponding author:

S. Bedra

Email: bedra_sami@yahoo.fr

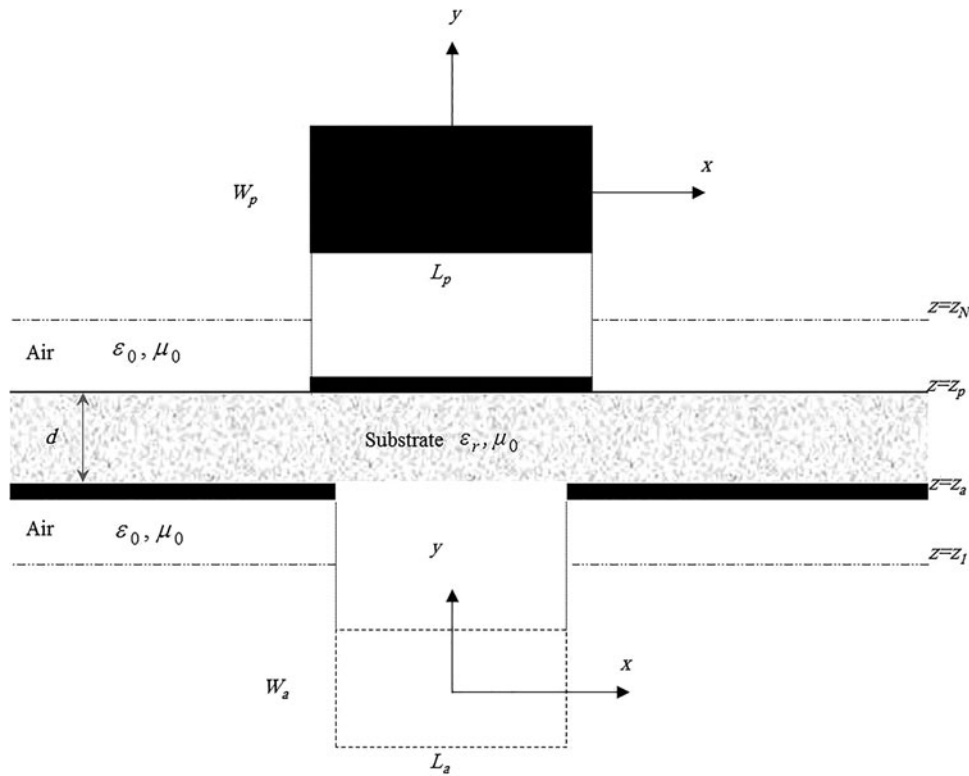


Fig. 1. Geometrical structure of a tunable rectangular microstrip patch over a ground plane with rectangular aperture.

the x -direction and width W_p along the y -direction over the ground plane with a rectangular aperture of length L_a and width W_a . Both the center of the patch and the center of aperture have the coordinate value $(x, y) = (0, 0)$. Also, the metallic patch and the ground plane are assumed to be perfect electric conductors of negligible thickness. The dielectric layer of thickness d is characterized by the free-space permeability μ_0 and the permittivity ϵ_r (ϵ_0 is the free-space permittivity and the relative permittivity ϵ_r can be complex to account for dielectric loss).

The ambient medium is air with constitutive parameters μ_0 and ϵ_0 . All fields and currents are time harmonic with the $e^{i\omega t}$ time dependence suppressed. The transverse fields inside the substrate region can be obtained via the inverse vector Fourier transforms as [5, 13]

$$\begin{aligned} \mathbf{E}(\mathbf{r}_s, z) &= \begin{bmatrix} E_x(\mathbf{r}_s, z) \\ E_y(\mathbf{r}_s, z) \end{bmatrix} \\ &= \frac{1}{4\pi^2} \int_{-\infty}^{+\infty} \int_{-\infty}^{+\infty} \bar{\mathbf{F}}(\mathbf{k}_s, \mathbf{r}_s) \cdot \mathbf{e}(\mathbf{k}_s, z) dk_x dk_y, \end{aligned} \tag{1}$$

$$\begin{aligned} \mathbf{H}(\mathbf{r}_s, z) &= \begin{bmatrix} H_y(\mathbf{r}_s, z) \\ -H_x(\mathbf{r}_s, z) \end{bmatrix} \\ &= \frac{1}{4\pi^2} \int_{-\infty}^{+\infty} \int_{-\infty}^{+\infty} \bar{\mathbf{F}}(\mathbf{k}_s, \mathbf{r}_s) \cdot \mathbf{h}(\mathbf{k}_s, z) dk_x dk_y, \end{aligned} \tag{2}$$

where $\bar{\mathbf{F}}(\mathbf{k}_s, \mathbf{r}_s)$ is the kernel of the vector Fourier-

transforming domain (VFTD) [5, 13]

$$\begin{aligned} \bar{\mathbf{F}}(\mathbf{k}_s, \mathbf{r}_s) &= \frac{1}{k_s} \cdot \begin{bmatrix} k_x & k_y \\ k_y & -k_x \end{bmatrix} \cdot e^{i\mathbf{k}_s \cdot \mathbf{r}_s}, \\ \mathbf{r}_s &= \hat{\mathbf{x}}x + \hat{\mathbf{y}}y, \mathbf{k}_s = \hat{\mathbf{x}}k_x + \hat{\mathbf{y}}k_y, k_s = |\mathbf{k}_s|. \end{aligned} \tag{3}$$

The relation which related the current $\mathbf{j}(\mathbf{k}_s)$, $\mathbf{j}_0(\mathbf{k}_s)$ on the conducting patch (ground plane with rectangular aperture) to the electric field on the corresponding interface $\mathbf{e}(\mathbf{k}_s, z_p)$, and $\mathbf{e}(\mathbf{k}_s, z_a)$ given by

$$\mathbf{e}(\mathbf{k}_s, z_p) = \bar{\mathbf{G}}(\mathbf{k}_s) \cdot \mathbf{j}(\mathbf{k}_s) + \bar{\Psi}(\mathbf{k}_s) \cdot \mathbf{e}(\mathbf{k}_s, z_a), \tag{4}$$

$$\mathbf{j}_0(\mathbf{k}_s) = -\bar{\Phi}(\mathbf{k}_s) \cdot \mathbf{j}(\mathbf{k}_s) - \bar{\mathbf{Y}}(\mathbf{k}_s) \cdot \mathbf{e}(\mathbf{k}_s, 0). \tag{5}$$

The four 2×2 diagonal matrices $\bar{\mathbf{G}}(\mathbf{k}_s)$, $\bar{\Psi}(\mathbf{k}_s)$, $\bar{\Phi}(\mathbf{k}_s)$, and $\bar{\mathbf{Y}}(\mathbf{k}_s)$ stand for a set of dyadic Green's functions in the vector Fourier transform domain. It is to be noted that $\bar{\mathbf{G}}(\mathbf{k}_s)$ is related to the patch current and $\bar{\mathbf{Y}}(\mathbf{k}_s)$ is related to the aperture field. $\bar{\Psi}(\mathbf{k}_s)$ and $\bar{\Phi}(\mathbf{k}_s)$ represent the interactions between the patch current and aperture field. In equations (5) and (6), the unknowns are $\mathbf{j}(\mathbf{k}_s)$ and $\mathbf{e}(\mathbf{k}_s, z_a)$. Another possible choice in the analysis of microstrip patches over the ground planes with apertures is to consider $\mathbf{j}_0(\mathbf{k}_s)$ as unknown instead of $\mathbf{e}(\mathbf{k}_s, z_a)$. It is anticipated, however, that a very large number of terms of basis functions would be needed for the expansion of the current $\mathbf{j}_0(\mathbf{r}_s)$ on the ground plane with aperture because of the wide conductor area. Hence, it is better to apply the Galerkin procedure to the unknown $\mathbf{E}(\mathbf{r}_s, z_a)$ field at the aperture [13].

The transverse electric field at the plane of the patch and the surface current density on the ground plane with a rectangular aperture can be obtained from equations (4) and (5), respectively, via the inverse vector Fourier transforms as

$$\mathbf{E}(\mathbf{r}_s, z_p) = \frac{1}{4\pi^2} \int_{-\infty}^{+\infty} \int_{-\infty}^{+\infty} \bar{\mathbf{F}}(\mathbf{k}_s, \mathbf{r}_s) \cdot [\bar{\mathbf{G}}(\mathbf{k}_s) \cdot \mathbf{j}(\mathbf{k}_s) + \bar{\Psi}(\mathbf{k}_s) \cdot \mathbf{e}(\mathbf{k}_s, z_a)] dk_x dk_y, \tag{6}$$

$$\mathbf{J}_o(\mathbf{r}_s) = -\frac{1}{4\pi^2} \int_{-\infty}^{+\infty} \int_{-\infty}^{+\infty} \bar{\mathbf{F}}(\mathbf{k}_s, \mathbf{r}_s) \cdot [\bar{\Phi}(\mathbf{k}_s) \cdot \mathbf{j}(\mathbf{k}_s) + \bar{\mathbf{Y}}(\mathbf{k}_s) \cdot \mathbf{e}(\mathbf{k}_s, z_a)] dk_x dk_y. \tag{7}$$

Boundary conditions require that the transverse electric field of equation (6) vanishes on the perfectly conducting patch and the current of equation (7) vanishes off the ground plane, to give the following coupled integral equations for the patch current and aperture field:

$$\int_{-\infty}^{+\infty} \int_{-\infty}^{+\infty} \bar{\mathbf{F}}(\mathbf{k}_s, \mathbf{r}_s) \cdot (\bar{\mathbf{G}}(\mathbf{k}_s) \cdot \mathbf{j}(\mathbf{k}_s) + \bar{\Psi}(\mathbf{k}_s) \cdot \mathbf{e}(\mathbf{k}_s, z_a)) dk_x dk_y = 0, \quad \mathbf{r}_s \in \text{patch}, \tag{8}$$

$$\int_{-\infty}^{+\infty} \int_{-\infty}^{+\infty} \bar{\mathbf{F}}(\mathbf{k}_s, \mathbf{r}_s) \cdot (\bar{\Phi}(\mathbf{k}_s) \cdot \mathbf{j}(\mathbf{k}_s) + \bar{\mathbf{Y}}(\mathbf{k}_s) \cdot \mathbf{e}(\mathbf{k}_s, z_a)) dk_x dk_y = 0, \quad \mathbf{r}_s \in \text{aperture} \tag{9}$$

The first step in the moment method solution of equations (8) and (9) is to expand both the patch current $\mathbf{j}(\mathbf{k}_s)$ and aperture field $\mathbf{E}(\mathbf{k}_s, z_a)$ as

$$\mathbf{j}(\mathbf{k}_s) = \sum_{n=1}^N a_n \begin{bmatrix} J_{xn}(\mathbf{r}_s) \\ 0 \end{bmatrix} + \sum_{m=1}^M b_m \begin{bmatrix} 0 \\ J_{ym}(\mathbf{r}_s) \end{bmatrix}, \tag{10}$$

$$\mathbf{E}(\mathbf{r}_s, z_a) = \sum_{p=1}^P c_p \begin{bmatrix} E_{xp}(\mathbf{r}_s) \\ 0 \end{bmatrix} + \sum_{q=1}^Q d_q \begin{bmatrix} 0 \\ E_{yq}(\mathbf{r}_s) \end{bmatrix}, \tag{11}$$

where J_{xn} , J_{ym} , E_{xp} , and E_{yq} are the known basis functions and a_n , b_m , c_p , and d_q are the mode expansion coefficients to be sought. Using the technique known as the moment method [13], with weighting modes chosen identical to the expansion modes, equations (8) and (9) are reduced to a system of linear

equations which can be written compactly in matrix form as

$$\begin{bmatrix} \begin{bmatrix} (\bar{\mathbf{U}}^{11})_{N \times N} & (\bar{\mathbf{U}}^{12})_{N \times M} \\ (\bar{\mathbf{U}}^{21})_{M \times N} & (\bar{\mathbf{U}}^{22})_{M \times M} \end{bmatrix} & \begin{bmatrix} (\bar{\mathbf{V}}^{11})_{N \times P} & (\bar{\mathbf{V}}^{12})_{N \times Q} \\ (\bar{\mathbf{V}}^{21})_{M \times P} & (\bar{\mathbf{V}}^{22})_{M \times Q} \end{bmatrix} \\ \begin{bmatrix} (\bar{\mathbf{W}}^{11})_{P \times N} & (\bar{\mathbf{W}}^{12})_{P \times M} \\ (\bar{\mathbf{W}}^{21})_{Q \times N} & (\bar{\mathbf{W}}^{22})_{Q \times M} \end{bmatrix} & \begin{bmatrix} (\bar{\mathbf{Z}}^{11})_{P \times P} & (\bar{\mathbf{Z}}^{12})_{P \times Q} \\ (\bar{\mathbf{Z}}^{21})_{Q \times P} & (\bar{\mathbf{Z}}^{22})_{Q \times Q} \end{bmatrix} \end{bmatrix} \cdot \begin{bmatrix} (\mathbf{a})_{N \times 1} \\ (\mathbf{b})_{M \times 1} \\ (\mathbf{c})_{P \times 1} \\ (\mathbf{d})_{Q \times 1} \end{bmatrix} = \mathbf{o}. \tag{12}$$

The elements of the matrix $(\bar{\mathbf{U}})_{(N+M) \times (N+M)}$, $(\bar{\mathbf{V}})_{(N+M) \times (P+Q)}$, $(\bar{\mathbf{W}})_{(P+Q) \times (N+M)}$, and $(\bar{\mathbf{Z}})_{(P+Q) \times (P+Q)}$ are given in [13].

It is easy to show that the entire matrix in equation (12) is a symmetric matrix. For the existence of a non-trivial solution of equation (12), we must have

$$\det(\bar{\mathbf{\Omega}}(f)) = 0, \quad \bar{\mathbf{\Omega}} = \begin{bmatrix} \bar{\mathbf{U}} & \bar{\mathbf{V}} \\ \bar{\mathbf{W}} & \bar{\mathbf{Z}} \end{bmatrix}. \tag{13}$$

Equation (13) is the characteristic equation for the complex resonant frequency $f = f_r + if_i$ of the generalized microstrip structure illustrated in Fig. 1. f_r is the resonant frequency and $2f_i/f_r$ is the half-power bandwidth of the structure.

In the following section, a basic ANN is described briefly and the application of neural network to the prediction the resonant characteristics of the microstrip antenna are then explained.

III. NEURAL NETWORK MODELING

ANN learns relationships among sets of input-output data which are characteristic of the device under consideration. It is a very powerful approach for building complex and non-linear relationship between a set of input and output data [14].

ANNs have been used frequently in signal-processing applications, speech and pattern recognition, remote sensing, etc. for the past two decades [15]. Ability, adaptive capability and ease of implementation have made ANN a popular tool for many design problems in today's communication world [9]. More importantly, ANNs can generalize and respond correctly to slightly deviant input values, not presented during the training process [16]. These networks directly give a good approximation of simulation and measured value, thereby avoiding the need for possibly a more complex and time-consuming conventional problem-specific algorithm [9]. In the present scenario, neural network models are used extensively for wireless communication engineering, which eliminates the complex and time-consuming mathematical and simulation procedures for designing antennas [10, 17, 18].

Multilayer perceptrons (MLPs) have been applied successfully to solve some difficult and diverse problems by training them in a supervised manner with a highly popular algorithm known as the error back propagation algorithm [19].

As shown in Fig. 2, the MLP consists of an input layer, one or more hidden layers, and an output layer. Neurons in the input layer only act as buffers for distributing the input

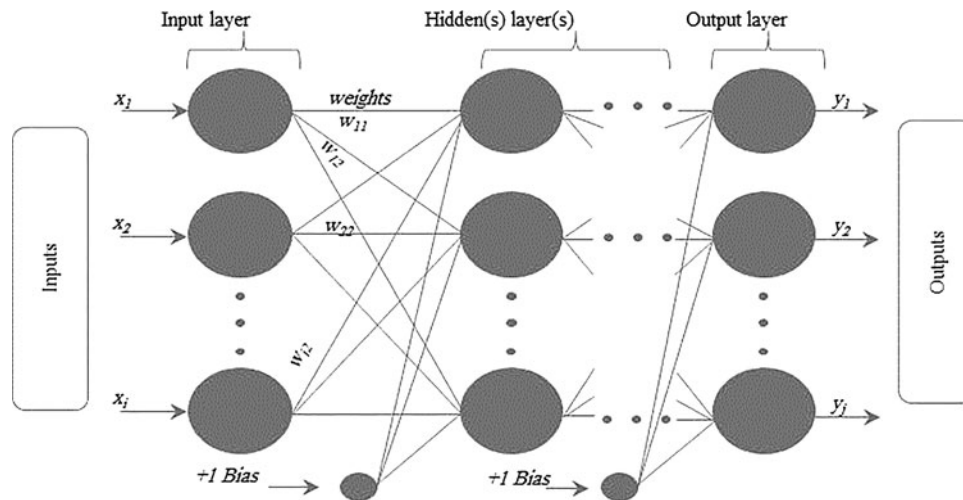


Fig. 2. General form of multilayered perceptrons.

signals x_i to neurons in the hidden layer. Each neuron in the hidden layer sums its input signals x_i after weighting them with the strengths of the respective connections w_{ji} from the input layer and computes its output y_j as a function f of the sum, namely

$$y_j = f\left(\sum w_{ji}x_i\right), \quad (14)$$

where f can be a simple threshold function or a sigmoid or hyperbolic tangent function [20]. The output of neurons in the output layer is computed similarly.

Training of a network is accomplished through adjustment of the weights to give the desired response via the learning algorithms. An appropriate structure may still fail to give a better model unless the structure is trained by a suitable learning algorithm. A learning algorithm gives the change $\Delta w_{ji}(k)$ in the weight of a connection between neurons i and j at time k . The weights are then updated according to the formula

$$w_{ji}(k+1) = w_{ji}(k) + \Delta w_{ji}(k+1). \quad (15)$$

MLP can be trained using many different learning algorithms [21]. In this paper, the following back propagation learning algorithm described briefly was used to train the MLP.

The back-propagation algorithm is based on the error correction learning rule. Basically, error back propagation learning consists of two passes through the different layers of the network, a forward pass and a backward pass. In the forward pass, an activity pattern applies to the sensor nodes of the network, and its effect propagates through the network layer by layer [21]. Finally, a set of outputs is produced as the actual response of the network. During the forward pass, the synaptic weights of the networks are all fixed. During the backward pass, on the other hand, all the synaptic weights are adjusted in accordance with an error correction rule. The actual response of the network is subtracted from a desired response to produce an error signal. This error signal is then propagated backward through the network against the direction of synaptic connections. The synaptic weights are adjusted to make the actual response of the network move closer to the desired response in a statistical

sense [19]. ANN model's accuracy depends on the amount of data presented to it during training. A well-distributed, accurately simulated or measured and sufficient data are the basic requirement to obtain an efficient model.

The data sets used in this paper were obtained from the method described in the previous section. A total of 250 data sets used to train the neuronal model. 112 data sets, which are completely different from training data sets, were used to test the neural network model. The most suitable network configuration found was 6, 12, 12, and 2 for the input layer, the first and second hidden layers, and the output layer, respectively. The tangent sigmoid and logarithmic sigmoid activation functions were used in the first and second hidden layers, respectively. The linear activation function was used in the input and output layers. Initial weights of the neural models were set up randomly, with learning rate = 0.5, goal = 0.0001, was trained for 5000 epochs. The CPU time taken by the spectral domain to give the both resonant frequency and half-power bandwidth for each input set is more than 5 min; it depends on three initial values used in Muller's algorithm for not seeking of the characteristic equation. The overall time to get the ANN trained is in the range of 3–4 h, depending on the required accuracy. All the numerical results presented in this paper we obtained on a Pentium IV computer with a 3.20-GHz processor and a total RAM memory of 2 GB.

The resonant characteristics of the antenna are obtained as a function of patch dimensions (L_p , W_p), aperture dimensions (L_a , W_a), height of the dielectric substrate (d), and dielectric constants of the material (ϵ_r) "see Fig. 3".

IV. NUMERICAL RESULTS AND DISCUSSION

One purpose of this work is to study the influence of some geometric parameters of the structure and the behavior of the final response. From these data an ANN is trained to predict the response of the structure due to the change of the considered parameter, within a given region of interest.

To confirm the computation accuracy, our numerical results are compared with experimental data previously published [22]. It can be clearly seen from Table 1 that our

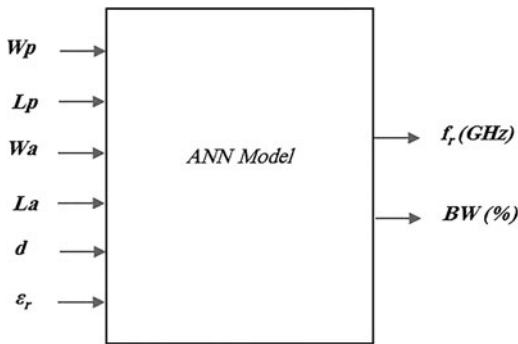


Fig. 3. Neural model for calculating the resonant frequency and half-power bandwidth of rectangular microstrip antenna without rectangular aperture in the ground plane.

Table 1. Comparison of measured and calculated resonant frequencies of a rectangular microstrip antenna with a rectangular aperture in the ground plane; $L_p \times W_p = 34 \text{ mm} \times 30 \text{ mm}$, $\epsilon_r = 2.62$.

Aperture dimension $L_a \times W_a \text{ (mm}^2\text{)}$	Substrate thickness $d \text{ (mm)}$	Resonant frequencies $f_r \text{ (GHz)}$	
		Measured [22]	Our results
7×0.7	0.794	2.896	2.901
10×1	3.175	2.750	2.770

results calculated using the neural model proposed in this paper are better than those predicted by other scientists. The very good agreement between the measured values and our computed resonant frequency values supports the validity of the neural model even with the limited data set.

With the aim of confirming the computation accuracy for the case of rectangular microstrip antenna (without aperture in the ground plane), we compare our results in Tables 2 and 3 with both experimental and theoretical data previously published [23–27]. The comparison is done for different antenna parameters.

From Table 2 it is observed that the bandwidths of a rectangular microstrip antenna computed by the present approach are closer to the experimental [23] and theoretical [24, 25] values. In Table 3, the resonant frequencies obtained by the present approach are compared with the previous results [26, 27]. The comparison shows that the resonant frequencies computed by the present method are in very good agreement with the measured data for a rectangular patch printed on a single substrate.

Table 2. Comparison of the calculated bandwidth with measured and calculated data, for a rectangular microstrip patch antenna without aperture in the ground plane, $\epsilon_r = 2.33$.

Input parameters (mm)		Bandwidth (%)				
		Measured	Calculated			
W_p	L_p	d	[23]	[24]	[25]	Our results
57	38	3.175	3.12	4.98	3.5	4.86
45.5	30.5	3.175	4.08	6.14	4.0	5.94
17	11	1.524	6.60	8.21	4.8	8.03

Table 3. Comparison of calculation and measured resonant frequencies for rectangular microstrip antenna without aperture in the ground plane; with $L_p = 25.08 \text{ mm}$, $W_p = 15.438 \text{ mm}$.

Input parameters		Resonant frequency $f_r \text{ (GHz)}$			
		Measured	Calculated		
$d \text{ (mm)}$	ϵ_r	[26]	[26]	[27]	Our results
0.84	2.2	6.057	6.092	6.15	6.063
1.64	2.2	5.887	5.883	5.89	5.885

In Fig. 4, we compare our results with theoretical data previously published [5]. The comparison is done in two different aperture dimensions. It can be seen that the resonant frequencies of the patches over the ground planes without aperture are larger than those obtained with aperture. These behaviors agree very well with those reported in the previous works [5, 13, 28].

Figure 5 predicts the influence of the aperture dimensions on the half-power bandwidth of the rectangular microstrip patch antenna for different antenna parameters. It can be seen that the bandwidth of the patches over the ground planes without aperture are larger than those obtained with aperture.

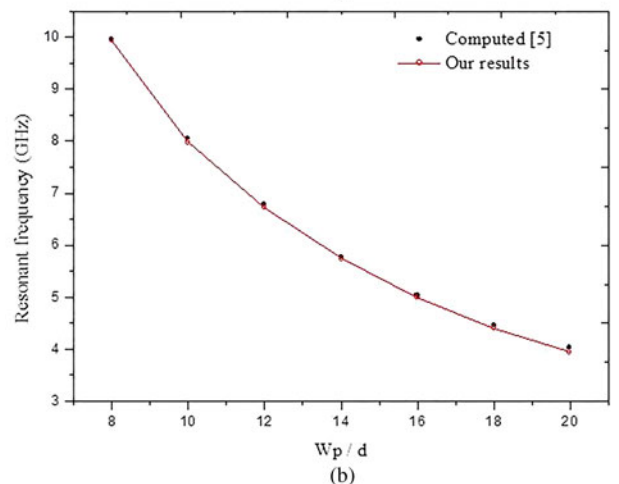
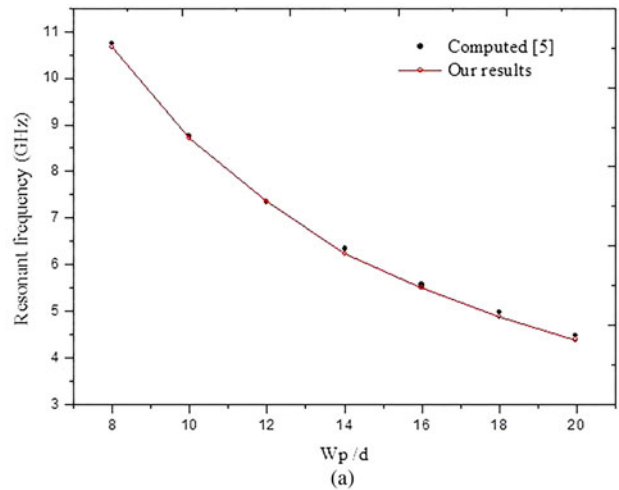


Fig. 4. Resonant frequencies of rectangular patches over the ground planes with and without rectangular apertures, (a) $L_a \times W_a = 0.25 W_p \times 0.5 W_p$, (b) $L_a \times W_a = 0.5 W_p \times 0.25 W_p$; $d = 1 \text{ mm}$, $\epsilon_r = 2.35$, $L_p = 1.5 W_p$.

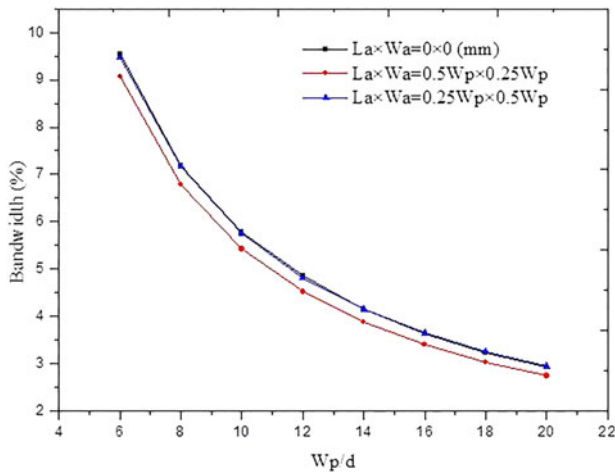


Fig. 5. Half-power bandwidths of rectangular patches over the ground planes with and without rectangular apertures; $d = 1$ mm, $\epsilon_r = 2.35$, and $L_p = 1.5 W_p$.

Figure 6 presents numerical results for the resonant frequencies of rectangular microstrip patches over the ground planes with and without rectangular apertures. Note that, the results obtained for the resonant frequencies without aperture ($W_a \times L_a = 0 \times 0$ mm²) lie around 10.89% above those obtained when $W_a \times L_a = 2 \times 4$ mm² and around 31.48% above those obtained when $W_a \times L_a = 4 \times 2$ mm².

In Fig. 7, the results are presented for the bandwidths of the rectangular microstrip patches analyzed in Fig. 1. As seen in Figs 6 and 7, the presence of the aperture has a stronger effect on the resonant characteristics. Thus, the differences between the results obtained for the half-power bandwidths when $W_a \times L_a = 0 \times 0$ mm² and those obtained when $W_a \times L_a = 2 \times 4$ mm² reach 8.55%, and reach 32.14% for those obtained when $W_a \times L_a = 4 \times 2$ mm². We conclude that the aperture length has a stronger effect on the resonant characteristics than the aperture width.

Figures 8 and 9, plots the radiation patterns in the E -plane ($\phi = 0$) and H -plane ($\phi = \pi/2$) of a rectangular microstrip patch over the ground planes with and without rectangular apertures in both the air half-space above the patch and the

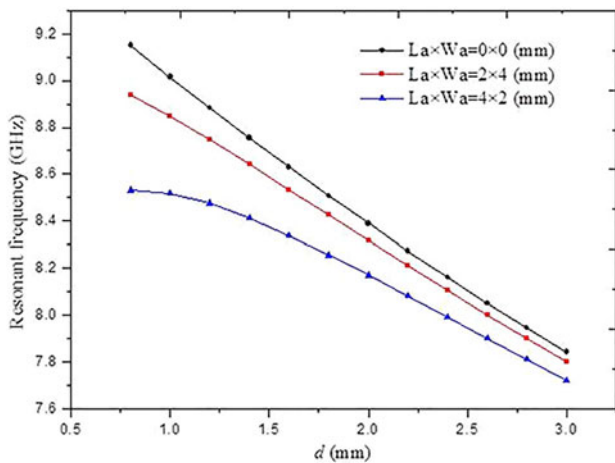


Fig. 6. Variation of the resonant frequencies of rectangular patches over the ground planes with and without rectangular apertures with the thickness of substrate; $\epsilon_r = 2.35$, $L_p = 15$ mm, and $W_p = 10$ mm.

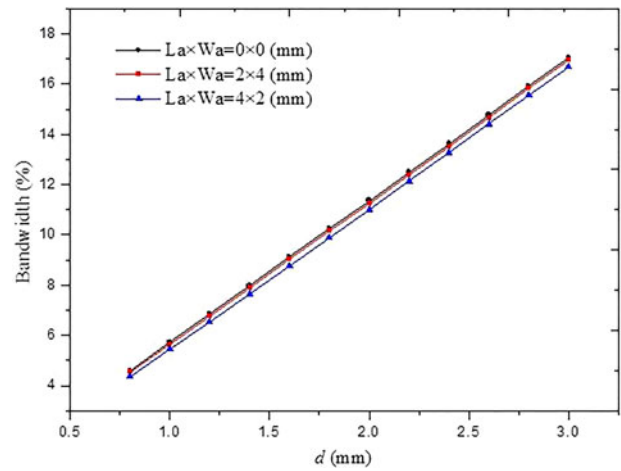


Fig. 7. Variation of half-power bandwidths of rectangular patches over the ground planes with and without rectangular apertures with the thickness of substrate; $\epsilon_r = 2.35$, $L_p = 15$ mm, and $W_p = 10$ mm.

air half-space below the ground planes. The structure without aperture in the ground plane operates at a frequency of 5.411 GHz. The resonant frequencies of the structures with an aperture in the ground planes are 5.348 and 5.124 GHz for the aperture dimensions of $L_a \times W_a = 0.2 W_p \times 0.2 W_p$ and

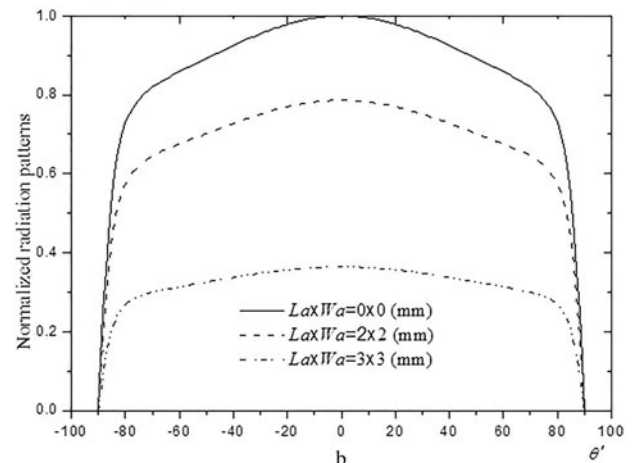
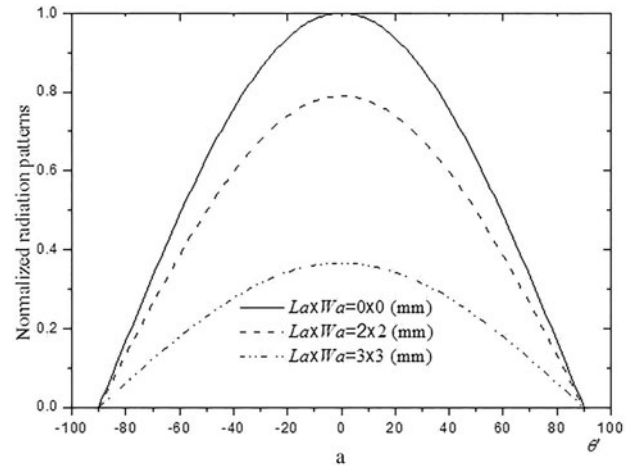


Fig. 8. Upper radiation patterns of rectangular patches over the ground planes with and without rectangular apertures (a) H -plane, (b) E -plane; with $L_p = 15$ mm, $W_p = 10$ mm, $\epsilon_r = 7$, and $d = 1$ mm.

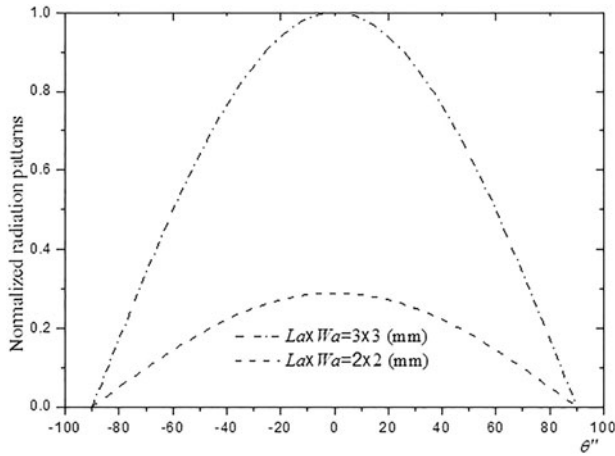


Fig. 9. Lower *H*-plane radiation pattern of rectangular patches over the ground planes with and without rectangular apertures; with $L_p = 15$ mm, $W_p = 10$ mm, $\epsilon_r = 7$, and $d = 1$ mm.

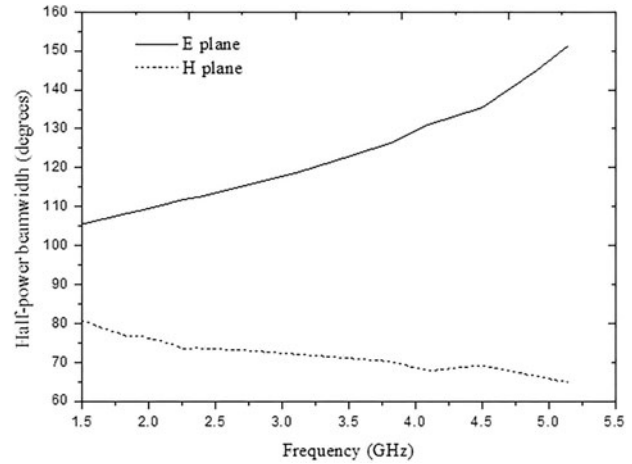


Fig. 10. Half-power beamwidth of rectangular antenna versus the resonant frequencies when L_p is varied; with $W_p = 57$ mm, $\epsilon_r = 2.33$, $d = 3.175$ mm, $L_a = 2$ mm, and $W_a = 2$ mm.

$L_a \times W_a = 0.3W_p \times 0.3W_p$, respectively. Concerning the radiation above the patch, it is clear that it decreases with the increase of the size of the aperture. On the other hand, increasing the size of the aperture increases the radiation below the ground plane. Therefore, the radiation back onto the forward ratio is particularly important as the size of the aperture is wider. Let us note that for apertures considered in Fig. 8, the back radiation is very weak in front of that forward. Obviously, the effects of the back radiation can be always suppressed by the investment of a supplementary conductive plan below the ground plane containing the apertures. Then the resonance properties of the microstrip patch are possible with a suitable choice of the separation between the additional conducting plane and the ground plane. This has been proven experimentally by Losada [29] for the case of a circular patch on the ground plane with circular apertures.

The variations of half-power beamwidth of the rectangular patch antenna with the resonant frequencies are shown in Fig. 10. The *E*-plane beamwidth of patch antenna increases by increasing the resonant frequencies, against the *H*-plane beamwidth decreases with increasing the resonance frequencies.

In Table 4, we compare our results obtained via the proposed neurospectral model with those obtained using the conventional SDA method. As well, to the resonant frequency and

half-power bandwidth, we have also shown the CPU time in this table. It is clear that our resonant frequencies and bandwidths coincide with those obtained by the conventional moment method. Note that, the time required for obtaining the resonant frequency and half-power bandwidth using the neurospectral model is much less in comparison to the spectral domain method.

V. CONCLUSION

A neural network-based CAD model can be developed for the analysis of a rectangular patch antenna, which is robust both from the angle of time of computation and accuracy. A distinct advantage of neuro-computing is that, after proper training, a neural network completely bypasses the repeated use of complex iterative processes for new cases presented to it. The single network structure can predict the results for patch antenna provided that input values are in the domain of training values. In the first example, a general design procedure for the microstrip antennas has been suggested using ANNs and this is demonstrated using the rectangular patch geometry. The spectral domain technique combined with the ANN method is several hundred times faster than the direct

Table 4. Comparison of our results obtained via the proposed neurospectral model with those obtained using the conventional spectral domain method, with $W_p \times L_p = 4 \times 2$ mm².

Input parameters				Conventional method (SDA)			Neurospectral method		
W_a (mm)	L_a (mm)	d (mm)	ϵ_r	Resonant frequency (GHz)	Bandwidth (%)	CPU time (min)	Resonant frequency (GHz)	Bandwidth (%)	CPU time (s)
2.5	2.5	0.6	2.35	8.956	3.382	5.39	8.972	3.365	0.0912
2.5	5	0.8	2.35	8.038	4.221	5.40	8.012	4.178	0.0914
5	2.5	1	2.35	8.710	5.621	5.43	8.731	5.642	0.0911
2.5	2.5	0.6	3.4	7.531	2.413	5.42	7.562	2.397	0.0915
2.5	5	0.8	3.4	6.784	2.931	5.40	6.778	2.894	0.0914
5	2.5	1	3.4	7.356	4.063	5.38	7.325	4.023	0.0912
2.5	2.5	1.2	10.3	4.365	1.394	5.38	4.352	1.412	0.0913
5	2.5	1.4	10.3	4.295	1.645	5.37	4.278	1.637	0.0912
2.5	5	1.8	10.3	4.057	2.053	5.41	4.036	1.997	0.0911

solution. This remarkable time gain makes the designing and training times negligible. Consequently, the neurospectral method presented is a useful method that can be integrated into a CAD tool, for the analysis, design, and optimization of practical shielded monolithic microwave-integrated circuit (MMIC) devices.

APPENDIX A

In this appendix, we appeared some details to reduce a system of linear equations which is written in Section II.

The elements of the matrix $(\bar{\mathbf{U}})_{(N+M) \times (N+M)}$, are given by

$$(\bar{\mathbf{U}}^{11})_{kn} = \int_{-\infty}^{+\infty} \int_{-\infty}^{+\infty} \frac{1}{k_s^2} [k_x^2 G^e + k_y^2 G^h] \tilde{J}_{xk}(-\mathbf{k}_s) \tilde{J}_{xn}(\mathbf{k}_s) dk_x dk_y, \tag{A.1}$$

$$(\bar{\mathbf{U}}^{12})_{km} = \int_{-\infty}^{+\infty} \int_{-\infty}^{+\infty} \frac{k_x k_y}{k_s^2} [G^e - G^h] \tilde{J}_{xk}(-\mathbf{k}_s) \tilde{J}_{ym}(\mathbf{k}_s) dk_x dk_y, \tag{A.2}$$

$$(\bar{\mathbf{U}}^{21})_{ln} = \int_{-\infty}^{+\infty} \int_{-\infty}^{+\infty} \frac{k_s k_y}{k_s^2} [G^e - G^h] \tilde{J}_{yl}(-\mathbf{k}_s) \tilde{J}_{xn}(\mathbf{k}_s) dk_x dk_y, \tag{A.3}$$

$$(\bar{\mathbf{U}}^{22})_{lm} = \int_{-\infty}^{+\infty} \int_{-\infty}^{+\infty} \frac{1}{k_s^2} [k_y^2 G^e + k_x^2 G^h] \tilde{J}_{yl}(-\mathbf{k}_s) \tilde{J}_{ym}(\mathbf{k}_s) dk_x dk_y. \tag{A.4}$$

In (A.1)–(A.4), \tilde{J}_{xn} and \tilde{J}_{ym} are the scalar Fourier transforms of J_{xn} and J_{ym} , respectively. The elements of the matrix $(\bar{\mathbf{V}})_{(N+M) \times (P+Q)}$ are given by

$$(\bar{\mathbf{V}}^{11})_{kp} = \int_{-\infty}^{+\infty} \int_{-\infty}^{+\infty} \frac{1}{k_s^2} [k_x^2 \psi^e + k_y^2 \psi^h] \tilde{J}_{xk}(-\mathbf{k}_s) \tilde{E}_{xp}(\mathbf{k}_s) dk_x dk_y, \tag{A.5}$$

$$(\bar{\mathbf{V}}^{12})_{kq} = \int_{-\infty}^{+\infty} \int_{-\infty}^{+\infty} \frac{k_x k_y}{k_s^2} [\psi^e - \psi^h] \tilde{J}_{xk}(-\mathbf{k}_s) \tilde{E}_{yq}(\mathbf{k}_s) dk_x dk_y, \tag{A.6}$$

$$(\bar{\mathbf{V}}^{21})_{lp} = \int_{-\infty}^{+\infty} \int_{-\infty}^{+\infty} \frac{k_s k_y}{k_s^2} [\psi^e - \psi^h] \tilde{J}_{yl}(-\mathbf{k}_s) \tilde{E}_{xp}(\mathbf{k}_s) dk_x dk_y, \tag{A.7}$$

$$(\bar{\mathbf{V}}^{22})_{lq} = \int_{-\infty}^{+\infty} \int_{-\infty}^{+\infty} \frac{1}{k_s^2} [k_y^2 \psi^e + k_x^2 \psi^h] \tilde{J}_{yl}(-\mathbf{k}_s) \tilde{E}_{yq}(\mathbf{k}_s) dk_x dk_y. \tag{A.8}$$

In (A.5)–(A.8), \tilde{E}_{xp} and \tilde{E}_{yq} are the scalar Fourier transforms of E_{xp} and E_{yq} , respectively. The elements of the

matrix $(\bar{\mathbf{W}})_{(P+Q) \times (N+M)}$ are given by

$$(\bar{\mathbf{W}}^{11})_{k'n} = \int_{-\infty}^{+\infty} \int_{-\infty}^{+\infty} \frac{1}{k_s^2} [k_x^2 \Phi^e + k_y^2 \Phi^h] \tilde{E}_{xk'}(-\mathbf{k}_s) \tilde{J}_{xn}(\mathbf{k}_s) dk_x dk_y, \tag{A.9}$$

$$(\bar{\mathbf{W}}^{12})_{k'm} = \int_{-\infty}^{+\infty} \int_{-\infty}^{+\infty} \frac{k_x k_y}{k_s^2} [\Phi^e - \Phi^h] \tilde{E}_{xk'}(-\mathbf{k}_s) \tilde{J}_{ym}(\mathbf{k}_s) dk_x dk_y, \tag{A.10}$$

$$(\bar{\mathbf{W}}^{21})_{l'p} = \int_{-\infty}^{+\infty} \int_{-\infty}^{+\infty} \frac{k_s k_y}{k_s^2} [\Phi^e - \Phi^h] \tilde{J}_{yl'}(-\mathbf{k}_s) \tilde{J}_{xp}(\mathbf{k}_s) dk_x dk_y, \tag{A.11}$$

$$(\bar{\mathbf{W}}^{22})_{l'm} = \int_{-\infty}^{+\infty} \int_{-\infty}^{+\infty} \frac{1}{k_s^2} [k_y^2 \Phi^e + k_x^2 \Phi^h] \tilde{E}_{yl'}(-\mathbf{k}_s) \tilde{J}_{ym}(\mathbf{k}_s) dk_x dk_y, \tag{A.12}$$

Finally, the elements of the matrix $(\bar{\mathbf{Z}})_{(P+Q) \times (P+Q)}$ are given by

$$(\bar{\mathbf{Z}}^{11})_{k'p} = \int_{-\infty}^{+\infty} \int_{-\infty}^{+\infty} \frac{1}{k_s^2} [k_x^2 Y^e + k_y^2 Y^h] \tilde{E}_{xk'}(-\mathbf{k}_s) \tilde{E}_{xp}(\mathbf{k}_s) dk_x dk_y, \tag{A.13}$$

$$(\bar{\mathbf{Z}}^{12})_{k'q} = \int_{-\infty}^{+\infty} \int_{-\infty}^{+\infty} \frac{k_x k_y}{k_s^2} [Y^e - Y^h] \tilde{E}_{xk'}(-\mathbf{k}_s) \tilde{E}_{yq}(\mathbf{k}_s) dk_x dk_y, \tag{A.14}$$

$$(\bar{\mathbf{Z}}^{21})_{l'p} = \int_{-\infty}^{+\infty} \int_{-\infty}^{+\infty} \frac{k_s k_y}{k_s^2} [Y^e - Y^h] \tilde{J}_{yl'}(-\mathbf{k}_s) \tilde{E}_{xp}(\mathbf{k}_s) dk_x dk_y, \tag{A.15}$$

$$(\bar{\mathbf{Z}}^{22})_{l'q} = \int_{-\infty}^{+\infty} \int_{-\infty}^{+\infty} \frac{1}{k_s^2} [k_y^2 Y^e + k_x^2 Y^h] \tilde{E}_{yl'}(-\mathbf{k}_s) \tilde{E}_{yq}(\mathbf{k}_s) dk_x dk_y. \tag{A.16}$$

APPENDIX B

To make the theoretical formulation more general and valid for various antennas structures (not only limited to single microstrip patch), the metallic patch is assumed to be embedded in a multilayered media consisting of N substrates with the optical axis normal to the patch (see Fig. 1 in [13]).

Once the complex resonance frequency is known, the eigenvector corresponding to the minimum eigenvalue of the matrix gives the coefficients of the current on the conductor patch and those of the electric field at the aperture on the ground plane. The method of stationary phase makes it

possible to obtain the following interface radiated in the upper half-space air of Fig. 1 in terms of the transverse electric field:

$$\begin{bmatrix} E_{\theta'}(r', \theta', \varphi') \\ E_{\varphi'}(r', \theta', \varphi') \end{bmatrix} = ik_0 \frac{e^{-ik_0 r'}}{2\pi r'} \begin{bmatrix} -1 & 0 \\ 0 & \cos \theta' \end{bmatrix} \cdot \mathbf{e}(\mathbf{k}_s, z_N), \tag{B.1}$$

where a local spherical coordinate system defined relative to the Cartesian $\{x' \equiv x, y' \equiv y, z' \equiv z\}$ system having an origin placed at the interface $z = z_N$ of Fig. 1 [13].

From equations (12 and 13 in [13]), we can obtain the transverse electric field $\mathbf{e}(\mathbf{k}_s, z_N)$ at the interface $z = z_N$ as a function of the transverse electric field $\mathbf{e}(\mathbf{k}_s, z_P)$ to the interface $z = z_P$ as follows [13]:

$$\mathbf{e}(\mathbf{k}_s, z_N) = [\bar{\Gamma}_>^{22} - \bar{\mathbf{g}}_0 \cdot \bar{\Gamma}_>^{12}]^{-1} \cdot \mathbf{e}(\mathbf{k}_s, z_P). \tag{B.2}$$

Taking into account (4.14) in [13] and (B.2), equation (B.1) becomes

$$\begin{bmatrix} E_{\theta'}(r', \theta', \varphi') \\ E_{\varphi'}(r', \theta', \varphi') \end{bmatrix} = ik_0 \frac{e^{-ik_0 r'}}{2\pi r'} [\bar{\Gamma}_>^{22} - \bar{\mathbf{g}}_0 \cdot \bar{\Gamma}_>^{12}]^{-1} \cdot \begin{bmatrix} -1 & 0 \\ 0 & \cos \theta' \end{bmatrix} \cdot [\bar{\mathbf{G}}(\mathbf{k}_s) \cdot \mathbf{j}(\mathbf{k}_s) + \bar{\Psi}(\mathbf{k}_s) \cdot \mathbf{e}(\mathbf{k}_s, z_1)]. \tag{B.3}$$

In equations (B.1) and (B.3), (k_x, k_y) are the points given by the stationary phase

$$k_x = -k_0 \sin \theta' \cos \varphi', \tag{B.4a}$$

$$k_y = -k_0 \sin \theta' \sin \varphi'. \tag{B.4b}$$

Unlike the method in which the equivalent limit the radiated field is calculated via recurrent formulas [29], the expression (B.3) allows the calculation of the radiated field in the upper half-space of the air in Fig. 1 using simple matrix multiplications.

Still based on the technique of the stationary phase, the radiated in the lower half-space air of Fig. 1 field can be obtained in terms of the transverse electric field at the interface $z = 0$ as follows:

$$\begin{bmatrix} E_{\theta''}(r'', \theta'', \varphi'') \\ E_{\varphi''}(r'', \theta'', \varphi'') \end{bmatrix} = ik_0 \frac{e^{-ik_0 r''}}{2\pi r''} \begin{bmatrix} -1 & 0 \\ 0 & \cos \theta'' \end{bmatrix} \cdot \begin{bmatrix} \cos 2\varphi'' & \sin 2\varphi'' \\ \sin 2\varphi'' & -\cos 2\varphi'' \end{bmatrix} \cdot \mathbf{e}(\mathbf{k}_s, 0), \tag{B.5}$$

where $\{r'', \theta'', \varphi''\}$ a local spherical coordinate system defined relative to the Cartesian $\{x'' \equiv x, y'' \equiv -y, z'' \equiv -z\}$ system having an origin placed at the interface of Fig. 1.

From equations ((10) and (16) in [13]), we can obtain the transverse electric field $\mathbf{e}(\mathbf{k}_s, 0)$ at the interface $z = 0$ as a function of the $\mathbf{e}(\mathbf{k}_s, z_1)$ transverse electric field to the interface $z =$

z_1 as follows:

$$\mathbf{e}(\mathbf{k}_s, 0) = [\bar{\mathbf{T}}_1^{11} - \bar{\mathbf{g}}_0 \cdot \bar{\mathbf{T}}_1^{12}]^{-1} \cdot \mathbf{e}(\mathbf{k}_s, z_1). \tag{B.6}$$

Substituting (B.5) into (B.6), equation (B.6) becomes

$$\begin{bmatrix} E_{\theta''}(r'', \theta'', \varphi'') \\ E_{\varphi''}(r'', \theta'', \varphi'') \end{bmatrix} = ik_0 \frac{e^{-ik_0 r''}}{2\pi r''} [\bar{\mathbf{T}}_1^{11} - \bar{\mathbf{g}}_0 \cdot \bar{\mathbf{T}}_1^{12}]^{-1} \cdot \begin{bmatrix} -1 & 0 \\ 0 & \cos \theta'' \end{bmatrix} \cdot \begin{bmatrix} \cos 2\varphi'' & \sin 2\varphi'' \\ \sin 2\varphi'' - \cos 2\varphi'' \end{bmatrix} \cdot \mathbf{e}(\mathbf{k}_s, 0). \tag{B.7}$$

In equations (B.6) and (B.7), (k_x, k_y) are the points given by the stationary phase

$$k_x = -k_0 \sin \theta'' \cos \varphi'', \tag{B.8a}$$

$$k_y = -k_0 \sin \theta'' \sin \varphi''. \tag{B.8b}$$

REFERENCES

- [1] Kumar, P.; Singh, G.: Theoretical investigation of the input impedance of gap-coupled circular microstrip patch antennas. *J Infrared Millim. Terahertz Waves*, **30** (11) (2009), 1148–1160.
- [2] Lei, L.; Korolkiewicz, E.; Ghassemlooy, Z.; Sambell, A.; Danaher, S.; Busawon, K.: Investigation of the equivalent circuit parameters and design of a dual polarised dual frequency aperture coupled microstrip antenna. *IEEE Trans. Antennas Propag.*, **61** (4) (2013), 2304–2308.
- [3] Liu, L.; Ghassemlooy, Z.; Sambell, A.; Danaher, S.; Smith, D.: Investigation of transformer turns ratio between feed and slot of aperture coupled slot antenna by using S_{11} parameter. *IEEE Trans. Antennas Propag.*, **61** (11) (2013), 5785–5787.
- [4] Vilovic, I.; Burum, N.; Brailo, M.: Microstrip antenna design using neural networks optimized by PSO, in 21st Int. Conf. Applied Electromagnetics and Communications, Dubrovnik, 2013.
- [5] Fortaki, T.; Khedrouche, D.; Bouttout, F.; Benghalia, A.: Numerical analysis of rectangular microstrip patch over ground plane with rectangular aperture. *Commun. Numer. Methods Eng.*, **20** (6) (2004), 489–500.
- [6] Ho, M.H.; Hsu, C.I.: Circular-waveguide-fed microstrip patch antennas. *Electron. Lett.*, **41** (22) (2005), 1202–1203.
- [7] Ye, Y.; Yuan, J.; Su, K.: A volume-surface integral equation solver for radiation from microstrip antenna on anisotropic substrate. *Int. J. Antennas Propag.*, **2012** (2012), 1–4.
- [8] Bhagat, P.P.; Pujara, D.; Adhyaru, D.: Analysis and synthesis of microstrip patch antenna using artificial neural networks, in IEEE Asia-Pacific Conf. Antennas and Propagation, Singapore, 2012.
- [9] Bose, T.; Gupta, N.: Design of an aperture-coupled microstrip antenna using a hybrid neural network. *Microw. Antennas Propag.*, *IET*, **6** (4) (2012), 470–474.
- [10] Mishra, R.; Patnaik, A.: Neurospectral computation for complex resonant frequency of microstrip resonators. *IEEE Microw. Guid. Wave Lett.*, **9** (9) (1999), 351–353.

- [11] Mishra, R.; Patnaik, A.: Neurospectral computation for input impedance of rectangular microstrip antenna. *Electron. Lett.*, **35** (20) (1999), 1691–1693.
- [12] Bedra, S.; Benkouda, S.; Fortaki, T.: Analysis of a circular microstrip antenna on isotropic or uniaxially anisotropic substrate using neurospectral approach. *COMPEL: Int. J. Comput. Math. Electr. Electron. Eng.*, **33** (1/2) (2013), 567–580.
- [13] Fortaki, T.; Benghalia, A.: Rigorous full-wave analysis of rectangular microstrip patches over ground planes with rectangular apertures in multilayered substrates that contain isotropic and uniaxial anisotropic materials. *Microw. Opt. Technol. Lett.*, **41** (6) (2004), 496–500.
- [14] Guney, K.; Yildiz, C.; Kaya, S.; Turkmen, M.: Artificial neural networks for calculating the characteristic impedance of air-suspended trapezoidal and rectangular-shaped microshield lines. *J. Electromagn. Waves Appl.*, **20** (9) (2006), 1161–1174.
- [15] Chopra, P.; Chandrasekhar, M.: Ann modeling for design of a matched low noise pHEMT amplifier for mobile application. *J. Comput. Electron.*, **12** (4) (2013), 743–751.
- [16] Kulshrestha, S.; Chheda, D.J.; Chakrabarty, S.; Jyoti, R.; Sharma, S.: Pole discontinuity removal using artificial neural networks for microstrip antenna design. *Int. J. Electron.*, **98** (12) (2011), 1711–1720.
- [17] Mishra, R.K.; Patnaik, A.: Neural network-based CAD model for the design of square-patch antennas. *IEEE Trans. Antennas Propag.*, **46** (12) (1998), 1890–1891.
- [18] Patnaik, A.; Mishra, R.K.: Ann techniques in microwave engineering. *IEEE Microw. Mag.*, **1** (1) (2000), 55–60.
- [19] Kumar, K.; Gunasekaran, N.: Bandwidth enhancement of a notch square shaped microstrip patch antenna using neural network approach, in *Int. Conf. Emerging Trends in Electrical and Computer Technology*, Tamil Nadu, 2011.
- [20] Guney, K.; Gultekin, S.: A comparative study of neural networks for input resistance computation of electrically thin and thick rectangular microstrip antennas. *J. Commun. Technol. Electron.*, **52** (5) (2007), 483–492.
- [21] Haykin, S.: *Neural Networks: a Comprehensive Foundation*, Prentice-Hall PTR, Upper Saddle River, NJ, USA, 1994.
- [22] Aksun, M.I.; Chuang, S.-L.; Lo, Y.T.: On slot-coupled microstrip antennas and their applications to CP operation-theory and experiment. *IEEE Trans. Antennas Propag.*, **38** (8) (1990), 1224–1230.
- [23] Chang, E.; Long, S.; Richards, W.: An experimental investigation of electrically thick rectangular microstrip antennas. *IEEE Trans. Antennas Propag.*, **34** (6) (1986), 767–772.
- [24] Chew, W.C.; Liu, Q.: Resonance frequency of a rectangular microstrip patch. *IEEE Trans. Antennas Propag.*, **36** (8) (1988), 1045–1056.
- [25] Pozar, D.M.: *PCAAD 3.0. Personal Computer Aided Antenna Design*, Antenna Design Associates, Inc., Leverett, MA, USA, 1996.
- [26] Aouabdia, N.; Belhadj-Tahar, N.-E.; Alquie, G.; Benabdelaziz, F.: Theoretical and experimental evaluation of superstrate effect on rectangular patch resonator parameters. *Prog. Electromagn. Res. B*, **32** (2011), 129–147.
- [27] Ansoft Corporation, Ansoft High Frequency Structure Simulator (HFSS) Version 13.0, Ansoft Corporation, Pittsburgh, PA, 2009.
- [28] Messai, A.; Benkouda, S.; Amir, M.; Bedra, S.; Fortaki, T.: Analysis of high superconducting rectangular microstrip patches over ground planes with rectangular apertures in substrates containing anisotropic materials. *Int. J. Antennas Propag.*, **2013** (2013), 1–7.
- [29] Losada, V.; Boix, R.R.; Horno, M.: Resonant modes of circular microstrip patches over ground planes with circular apertures in multilayered substrates containing anisotropic and ferrite materials, *IEEE Transact. Microw. Theory Tech.*, **48** (10) (2000), 1756–1762.

Lotfi Djouane was born in Batna, Algeria, in 1980. He received his Master Science and Ph.D. degrees in Electronics Engineering from the University of Batna, Algeria, in 2006 and 2009, respectively. Currently, he is an Associate Professor in the Department of Electronics at M'sila University, Algeria. He has published five papers in refereed journals and more than ten papers in conference proceedings. His main research deals with numerical methods and microstrip antennas.

Sami Bedra was born on August 3, 1984 in Batna, Algeria. He obtained his Engineer and Master Science degrees both in Electronics from the University of Batna, Algeria, in 2008 and 2011, respectively. He is currently working toward the Ph.D. degree at the University of Batna. His current research activities include neural network, optimization techniques, and their applications to patch antennas.

Randa Bedra was born on September 9, 1989 in Batna, Algeria. She received her Master Science in Microwave and Telecommunications from the University of Batna, Algeria, in 2013. She is currently with the Laboratory of Advanced Electronics at the Electronics Department, University of Batna, Batna, Algeria. She is currently working toward the Ph.D. degree at the University of Batna. Her main research deals with numerical methods and microstrip antennas.

Tarek Fortaki was born on March 31, 1972 in Constantine, Algeria. He received his Engineer of Communication degree in 1995, the Master Science degree in Microwaves in 1999, and the Doctorate degree in Microwaves in 2004, all from the Electronics Department, Faculty of Engineering Science, University of Constantine. Currently, he is a Professor at the Electronics Department, Faculty of Engineering Science, University of Batna. He has published 17 papers in refereed journals and more than 40 papers in conference proceedings. He serves as reviewer for several technical journals. His main interests are electromagnetic theory, numerical methods and modeling of antennas, and passive microwave circuits.